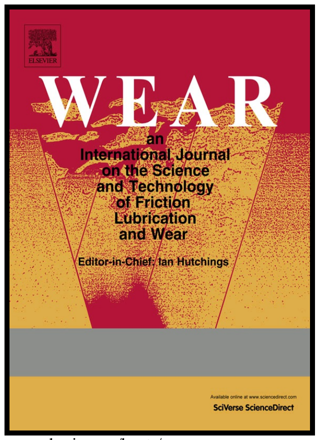

High speed observation of damage created by a collapse of a single cavitation bubble

Matevž Dular, Tomaž Požar, Jure Zevnik, Rok Petkovšek

PII: S0043-1648(18)30804-4
DOI: https://doi.org/10.1016/j.wear.2018.11.004
Reference: WEA102539

To appear in: *Wear*

Received date: 16 July 2018
Revised date: 17 October 2018
Accepted date: 7 November 2018

Cite this article as: Matevž Dular, Tomaž Požar, Jure Zevnik and Rok Petkovšek, High speed observation of damage created by a collapse of a single cavitation bubble, *Wear,* https://doi.org/10.1016/j.wear.2018.11.004

High speed observation of damage created by a collapse of a single cavitation bubble

[1]Matevž Dular*, [1]Tomaž Požar, [1]Jure Zevnik, [1]Rok Petkovšek

[1]Faculty of Mechanical Engineering, University of Ljubljana, Askerceva 6, 1000 Ljubljana, SI-Slovenia, matevz.dular@fs.uni-lj.si

Abstract

One of the remaining open questions in cavitation erosion research is the one on the importance of the microjet and the shock wave on the formation of the pit. Up until now, no successful attempt has been made to study this in detail, mainly because the damage could only be detected and evaluated after several successive bubble collapses.

A bubble with a maximum diameter of up to 3.3 mm was created during photoionization using a Nd:YAG laser. The damage was observed on a 9 µm thick aluminum foil attached to a glass substrate. Two high speed cameras were simultaneously used. One captured the dynamics of the bubble, while the other recorded the damage of the foil.

We also observed the collapse of a bubble in the presence of shear flow, where most of the damage is created by the microjet mechanism. Sometimes, the collapse of the bubble rim, at the rebound of the initial bubble causes pits in a well-known circular pattern. From the recordings at the very fastest acquisition rate, we determined that the material deforms and then partially relaxes, while a significant deformation remains. The whole process is only 2-3 µs long.

Graphical abstract:

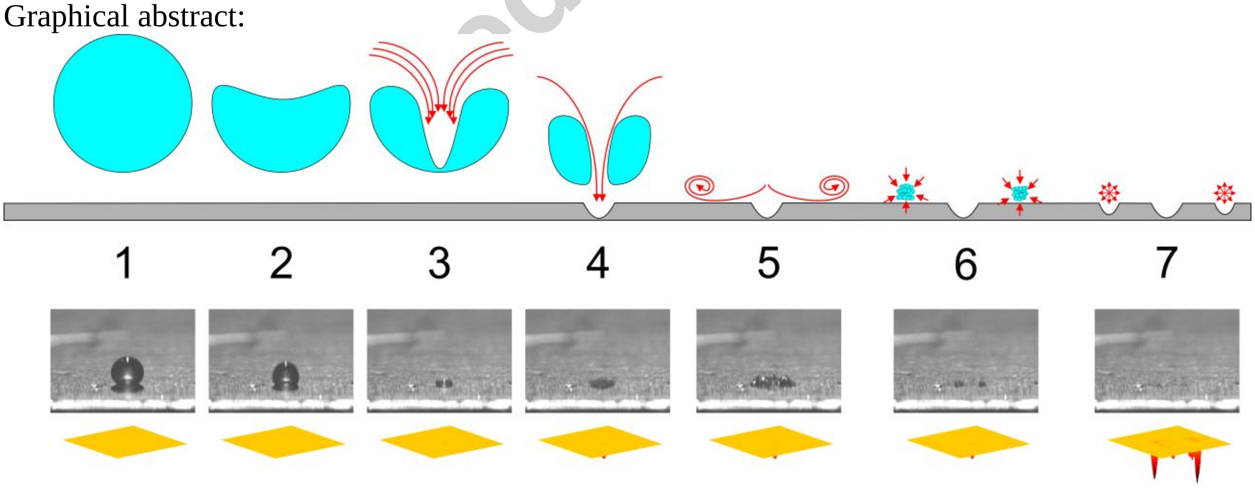

Keywords: cavitation; erosion; single bubble; shear flow; high speed observation

1 Introduction

Currently, the most widely accepted explanation for the occurrence of cavitation erosion is that the potential energy contained in a macro cavity is transformed into the radiation of acoustic pressure waves, and further on into the erosive potential contained in the micro scale cavitation structures or single bubbles that collapse in the vicinity of the material boundaries [1].

Two theories describe the last stages of life of a micro-scale cavitation structure:

- the micro jet [2],
- the spherical micro bubble collapse [3].

Figure 1 schematically shows both processes.

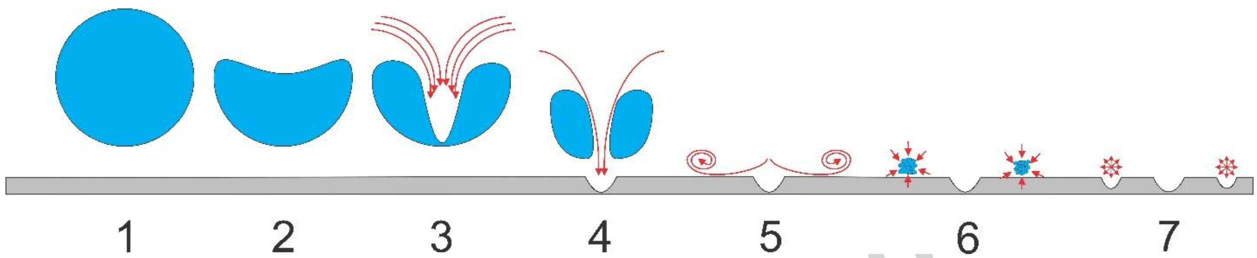

Figure 1: Two possible mechanisms of cavitation erosion.

The bubble reaches it maximal size (1). Due to the vicinity of the rigid surface, its upper boundary collapses faster than the one closer to the wall (2 and 3). A microjet forms (3), which can reach a velocity of several hundred m/s. When it hits the solid surface, a water hammer pressure occurs (Eqn. 2), which is high enough to deform the surface (4). After the microjet-induced collapse, the flow moves radially outwards (5) causing a secondary evaporation, or "splashing" (6) [4]. This results in a number of very small bubbles (μm size), which, due to surface tension forces, preserve their spherical shape during the collapse. This results in the formation of significant shock waves, which can again reach amplitudes, capable of deforming the material (7).

One of the first observations of a single bubble collapse was the one performed by Blake and Gibson [5], which has evidently shown the formation of a microjet. It was found that the liquid jet that penetrates the bubble can reach a velocity of several hundred m/s. The value can be estimated from the Kelvin impulse and, to a certain accuracy, follows the relation given by [6]:

$$v_{jet} = 8.97\gamma^2 \sqrt{\frac{\Delta p}{\rho}}, \qquad (1)$$

where γ is the nondimensional distance of the bubble center from the surface ($\gamma = h/R$, where h is the distance and R is the bubble radius). The pressure, which exerted to the surface is related to the water hammer stress [6], which is, if the density and the sonic velocity of the solid are large compared to the density and the sonic velocity of the liquid, defined as:

$$p = \eta \cdot \rho \cdot c \cdot v\,, \qquad (2)$$

with η being the efficiency of the energy transfer, estimated to η=0.6 by Chahine [7]. The maximal value will lie in the order of a GPa, high enough to cause damage to the material. The water hammer pressure is sustained for a short period of time – the time needed for the impact signal to traverse the radius of the jet, which is in the order of a microsecond. After that, a much smaller, stagnation pressure is established.

The splashing phenomenon, the secondary evaporation in a ring like form, due to high shear in the vicinity of the wall, was first described by Tong et al. [4], while Hansson et al. [8] predicted the shock waves which originate from the collapse of the cloud of bubbles. These waves are launched during the collapse of spherical microbubbles which forme a ring and can be estimated by simply calculating the Rayleigh-Plesset equation (the bubbles remain spherical throughout their lifetime). Again, the value is in the order of GPa, which can cause failure of the material.
The dynamics of bubbles near the surface was extensively investigated in the past, both experimentally and numerically. Studies of the damage caused by single bubble collapses are less common. Philipp and Lauterborn [9] made a breakthrough by their investigation where the damage was studied after several hundred bubble collapses. They concluded, based on a posterior measurement of the damage, that both mechanisms, the microjet and the spherical collapse of microbubbles contained in the ring cavity play a role in the process. Their influence depends on the standoff distance of the bubble.

One of the arguments that a micro-jet cannot be the responsible for the majority of the damage is the presence of the shear flow in many applications, which suffer from cavitation erosion (pumps, propellers, turbines). If a bubble is exposed to shear forces, the jet will deviate from the direction perpendicular to the surface and its impact will be less aggressive [10].

If there is indeed a significant difference between the damage mechanisms for the cases with and without the presence of the shear flow, this could also explain why in some cases results from vibratory erosion test (such as ASTM G32 (2016)), where there is an absence of shear flow, do not relate well to the tests in real condition, where shear flow is present.

Which mechanism is more pronounced (microjet or the microbubble ring collapse) was until now impossible to determine directly. To investigate this issue, we developed of a novel technique, that enables a simultaneous observation of bubble collapse and the deformation of the surface, by using two high speed cameras [12], [13]. In addition, we also investigate the mechanisms in the presence of shear flow.

2 Experiment

2.1 Experimental set-up

Figure 2 shows the schematics of the experimental set-up.

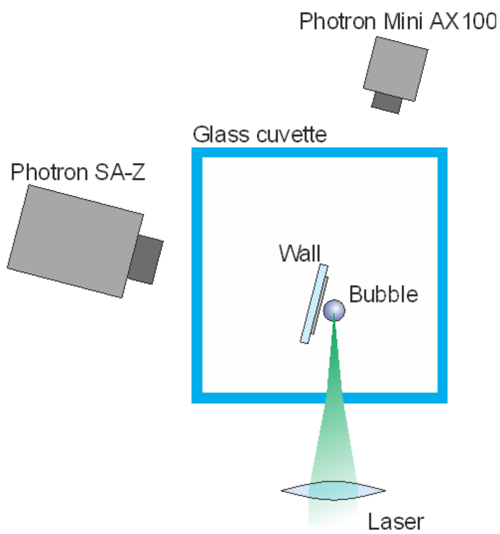

Figure 2: Experimental set-up.

Nd:YAG laser pulses with 1064 nm wavelength were used to initiate the bubble growth. The output energy of the 5 ns long pulse was maximally 16 mJ, which, due to the absorption of light on its path in the liquid corresponds to 10 mJ at the position of the breakdown. The focusing optics has been designed for relatively low aberrations, cone angle was 12° in water. The “standard” bubble with the diameter of 3.3 mm was generated 20 mm from the wall of the glass cuvette. The time of the bubble collapse when no wall was present was 147 μs and varied somewhat depending on the distance from the wall.

Water quality is an issue in cavitating flow, but less so, when dealing with single bubble dynamics (when it is not extremely altered). Of course, there were studies [14], [15] , that showed that when a bubble grows inside a bubbly medium (highly deteriorated water quality) a noticeable reductions in both the maximum achieved primary bubble radius and bubble period are seen. In the present study distilled water was used. Tests with additionally degassed water did not reveal any difference in the dynamics, hence untreated water was used further on.

In addition to stationary experiments, a set of tests in the presence of shear flow was performed. This is an important issue, as in the applications (turbines, pumps, propellers), the bubbles might be carried by the flow as they collapse, and the process might differ from the one where the bubble is at rest. The flow was introduced by a circulation pump. The nozzle (10 mm diameter) was positioned at a distance of 7 mm from the plasma breakdown so that the flow would carry the bubble in the direction parallel to the wall. The flow rate was measured by ABB ProcessMaster 610 DN meter with an uncertainty of less than 1 % of the measured value.

Two high speed cameras were used. In most cases, the slower, Photron Mini AX100, was used to observe the bubble dynamics, while the faster, Photron S-Z type 2100K-M-64GB, was used to simultaneously measure the deformation of the aluminum foil.

2.2 Aluminum foil as an erosion sensor

The idea of the experiment was to simultaneously record images of the cavitation bubble and the cavitation damage [12], [13]. The view of the upper side of the foil is obstructed by the bubble, hence one needs to look at the foil from the bottom side to see the damage during the presence of the bubble. Consequently, a glass plate was used for the wall and, equally important, the foil had to be thin enough so that the cavitation damage, which occurs on the side exposed to cavitation bubble, was also visible on the other side (Fig. 3).

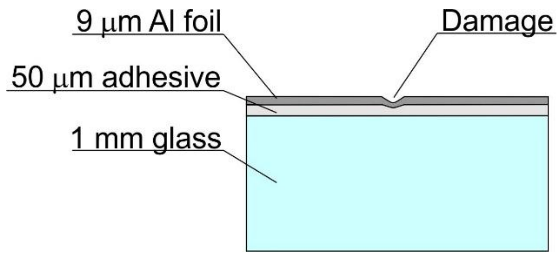

Figure 3: Side-view of the erosion-sensitive "specimen".

We have chosen a 9-μm-thick aluminum foil and attached it to the 1-mm-thick microscope glass slide by an optically clear two-sided adhesive tape with a thickness of 50 μm (Fig. 3).

2.3 Damage detection

Since we are observing the foil with a camera, only the surface of the damaged area can be accurately measured. Based on our previous experience and development of the SFS (Shape From Shading) algorithm [16] we were also able to qualitatively and partially quantitatively reconstruct the 3 dimensional shape of the cavity.

For the present evaluation, we used an approach that combines several evaluation procedures used before [12], [17]. We evaluated the images in pairs – the intensity of every pixel of the image at the time t was subtracted from the intensity of the same pixel at time $t+\Delta t$, thus eliminating most of the surface and illumination imperfections. Then we employed the pit-count method [18] which determines the pits in an image - from each image pair we obtained the number and the area of newly appeared pits. The pit-count method gives a distribution of the number and the area of the pits and consequently, the distribution of the magnitude of cavitation damage on the surface. We can also determine the distribution of the size of the pits. Since we were comparing pairs of two successive images, we were also able to obtain the information of the pit overlapping.

Images of the aluminum foil were treated as matrices A with $i \times j$ elements ($A(i,j) \in \{0,1,...255\}$) with 8-bit values which can range from 0 (black) to 255 (white). Erosion was evaluated in image pairs: image matrix at time $t+\Delta t$ was subtracted from image matrix at time t ($B(i,j,t)= A(i,j,t) - A(i,j,t+\Delta t)$). This way a new matrix B was obtained. When the matrix element $B(i,j)$ did not change between times t and $t+\Delta t$ its value was 0 ($B(i,j,t)=0$). When the change occurred, the value was $B(i,j,t)\neq 0$. Since small changes could be present due to insignificant changes in illumination, vibration etc., damage was only considered when a certain change threshold was exceeded (more than 5% of decrease or increase in brightness). The number of the pits, their size and overall damaged area could then be determined. More details on the methodology can be found in previous papers by Petkovsek and Dular [12].

2.4 Pit geometry reconstruction

In the present study, the shape in question is constantly changing but the texture remains unchanged. Based on our previous positive experience [17], the shape from shading algorithm was used to reconstruct the shape from images.

2.4.1 The algorithm

We assume that the surface under consideration is of a uniform albedo and reflectance, and that the light source directions and camera positions are known. Under the assumptions of distant light sources and observer, the variation in intensity become purely a function of the local surface orientation.

$$I(x,y)=\mathrm{R}\big(p(x,y),\mathrm{q}(x,y)\big), \tag{3}$$

where *(p, q) = (z*$_x$ *, z*$_y$*)* are the depth map derivatives and *R(p, q)* is called the reflectance map, which is defined as the non-negative dot product between the surface normal $\hat{n}=(p,q,1)/\sqrt{1+\mathrm{p}^2+\mathrm{q}^2}$ and the light source direction $\mathrm{v}=\left(v_x,\mathrm{v}_y,\mathrm{v}_z\right)$:

$$R(p,q)=\max\left(0,\rho\,\frac{pv_x+qv_y+v_z}{\sqrt{1+p^2+q^2}}\right), \tag{4}$$

where *r* is the surface reflectance factor (albedo). Eqns. 1 and 2 can be used to estimate *(p,q)* using the non-linear least squares method. But additional constraints have to be imposed, since there are more unknowns per pixel *(p,q)* than there are measurements *(I).* Instead of first recovering the orientation fields *(p,q)* and integrating them to obtain a surface, we can directly minimize the discrepancy in the image formation (Eqn. 1) while finding the optimal depth map *z(x,y)* [19].

Once the surface normals or gradients have been recovered at each pixel, they can be integrated into a depth map using a variant of regularized surface fitting [20].

The accuracy of the SFS method was tested on a reconstruction of the shape of a single cavitation indentation (Fig. 4). The results of geometry reconstruction by SFS were compared with the ones obtained by the interferometric measuring technique, which permits 3 dimensional determination of the shallow indentations including quantitative information about their size. In Fig. 4a, 3D optical microscope Bruker - ContourGT-K0 was used which enables the resolution of the shape reconstruction of up to 40 nm in lateral and 0.1 nm vertical direction. In this specific case, the lateral sampling step was 1.3 µm at the approximate vertical resolution of under 10 nm [21].

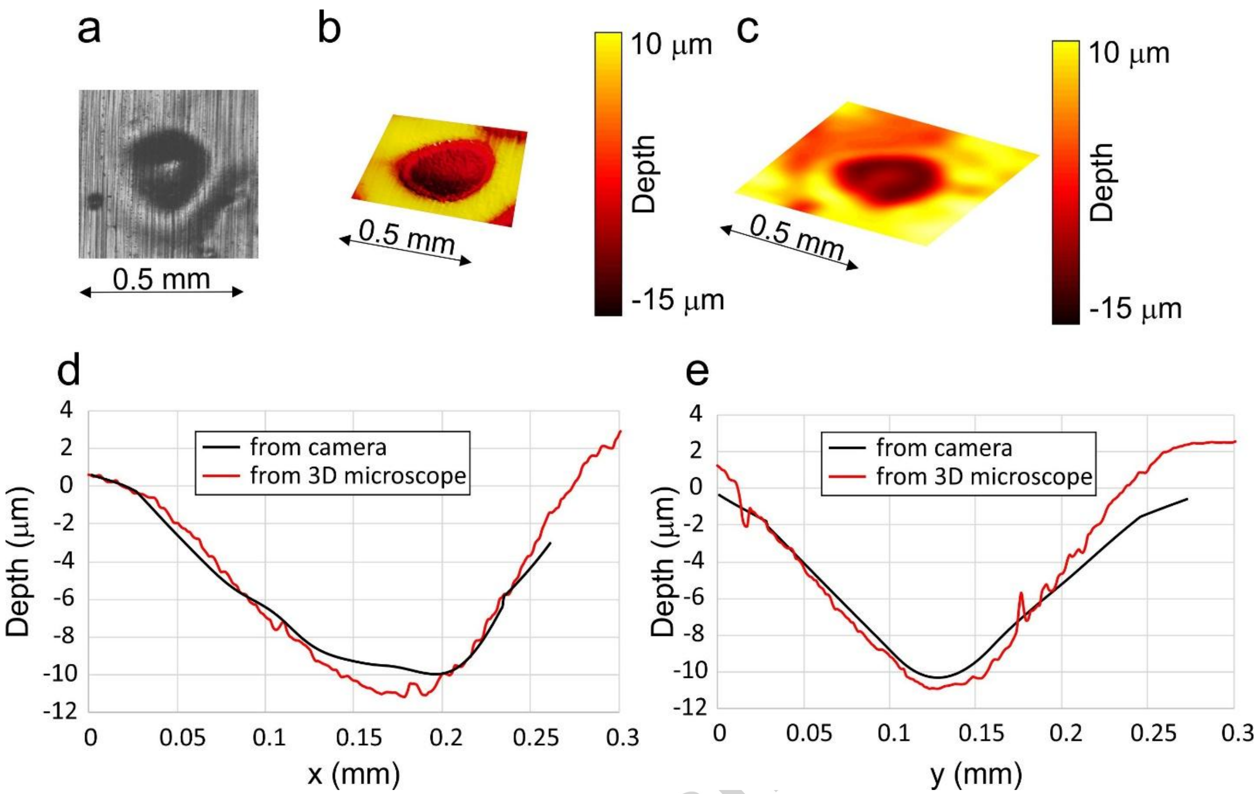

Fig. 4: Comparison between interferometric and SFS shape reconstruction.

Figure 4 shows the comparison between interferometric and SFS shape reconstruction. (a) shows the raw image of a single cavitation pit, (b) is the 3D representation obtained from the interferometric microscope and (c) is the 3D shape determined by the SFS algorithm. (d) and (e) show the measured cross-sections in two directions through the deepest part of the pit.

From the comparison we see that there are some discrepancies between the two measuring methods. The resolution of the SFS method is not as good as the one using the interferometric method, and thus the pit appears smoother when SFS is used. Nonetheless, the general topology is well determined, and the maximal depth agrees well. The analysis show that the shape of the pit obtained by the SFS method can be determined within about 15% to the interferometric one. This value is relatively large, but still suitable for the present study, where we focus more on the mechanisms that cause the damage and not as much on the details of the topology of the damage itself.

2.5 Investigated conditions

We investigated an ensemble of conditions, where the distance of the bubble with the radius (r) from the wall (h) was changed from $\gamma = \frac{h}{r}$ = 0.05… 3.0, with the interval of approximately 0.18. For each case 50 repetitions were made.

Two sets of measurements were made – the first one at stationary conditions, and the second one, where local shear flow (5 m/s) was introduced to investigate the influence of the shear forces on the specifics of bubble collapse and the induced damage.

3 Results

The research consists of a significant number of experiments, while only the representative are presented here in more detail. In all cases (Figs. 5-10) the upper sequence shows the bubble behavior recorded by the primary camera. The bottom sequence is the result of the damage evaluation (Sec. 2.4) from the images recorded by the secondary camera.

3.1 Bubble collapse at stationary conditions

3.1.1 Bubble in a close vicinity of the wall (γ=0.05)

First, the results of measurements in the close vicinity of the wall are presented (Fig. 5).

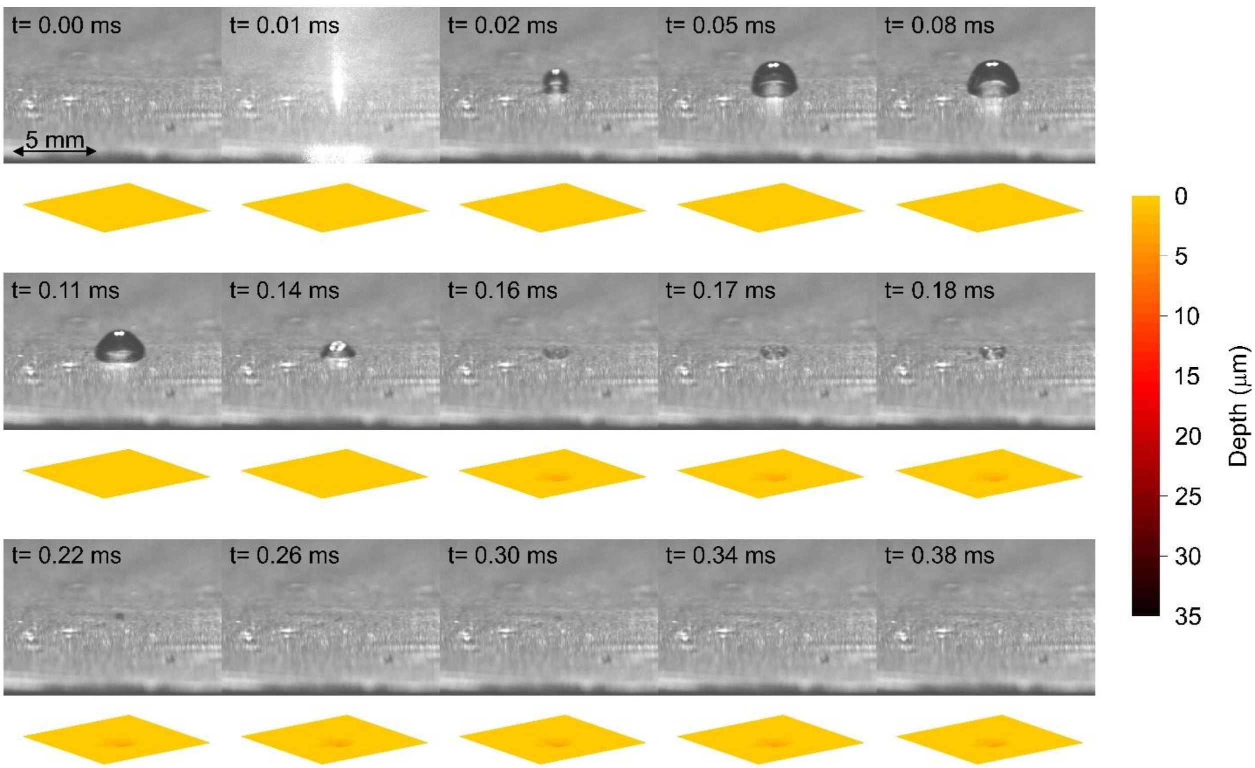

Fig. 5: Bubble and damage for collapse in the close vicinity of the wall (γ =0.05).

The plasma was initiated at the closest possible distance from the wall (γ =0.05). As one can see from the frame taken at t=0.01 ms no damage was caused by the laser pulse. The bubble reaches the maximal size of r=1.6 mm at t=0.08 ms and features a shape of an almost perfect half sphere at that moment. It collapses at t=0.16 ms in a form of a microjet, what causes a formation of a pit at that moment. Its depth is estimated to 10 μm. The damaged area has a comparable size to the bubble shortly before the collapse, which also corresponds well to the diameter of the microjet. The bubble later (until t= 0.22 ms) undergoes a non-distinctive splashing, a secondary evaporation, which is not pronounced enough to cause additional damage.

3.1.2 Bubble in a vicinity of the wall (γ=0.90)

Figure 6 shows the growth and the collapse of a bubble somewhat further from the wall (γ=0.90).

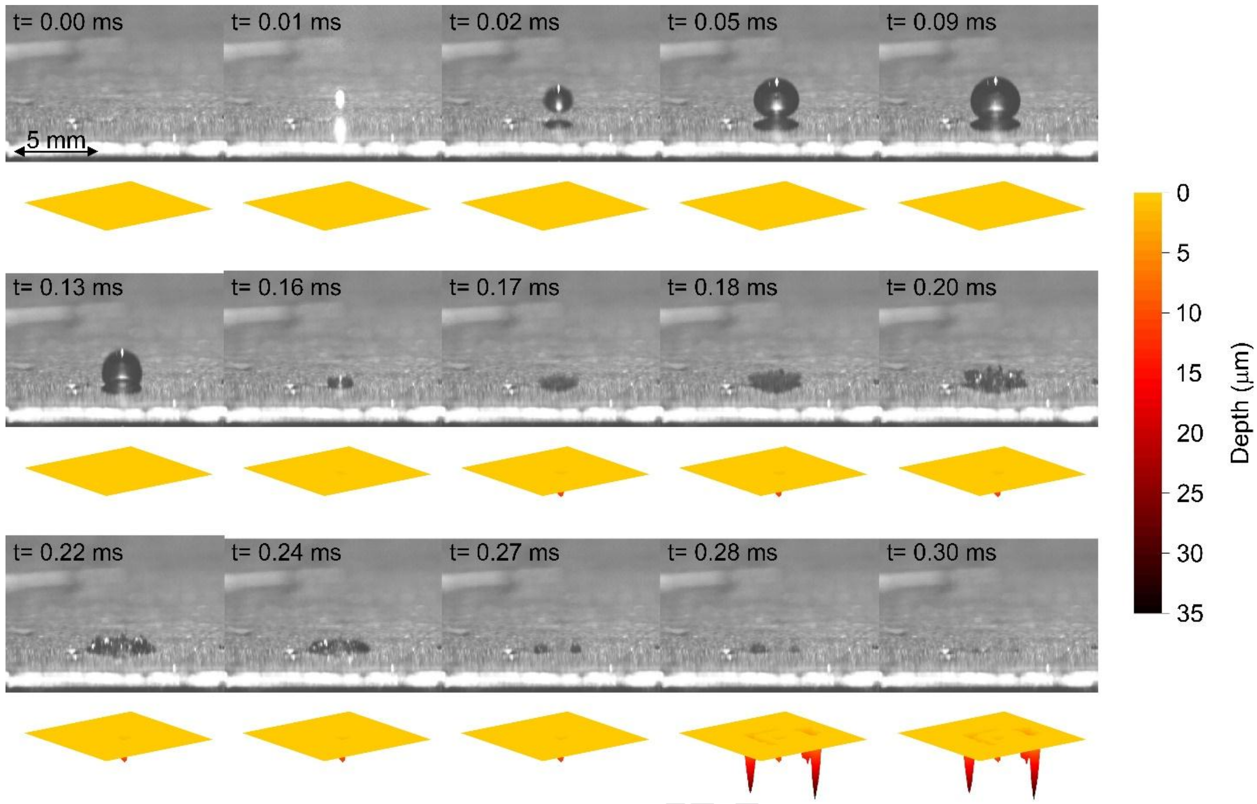

Fig. 6: Bubble and damage for collapse in the vicinity of the wall (γ =0.90).

This time, the laser pulse at t=0.01 ms was focused a bit further from the wall. The bubble contacts the wall just prior it reaches its maximal size (r = 1.6 mm) at about t=0.08 ms. The collapse in a form of a microjet again occurs at t=0.16 ms. In this case, the damaged area is smaller, but the pit is deeper, about 15 μm. The bubble then splashes, and one can see a violent collapse of the vapor ring at t=0.28 ms. This causes further damage to the foil which corresponds to the shape of the vaporous ring before the collapse. The damage is more pronounced than the one caused by the microjet, with the maximal depth in the order of 35 μm.

3.1.3 Bubble away from the wall (γ =1.90)

Figure 7 shows the temporal evolution of the bubble and the corresponding damage for the case further away from the wall, when the bubble, as it grows, does not touch the wall.

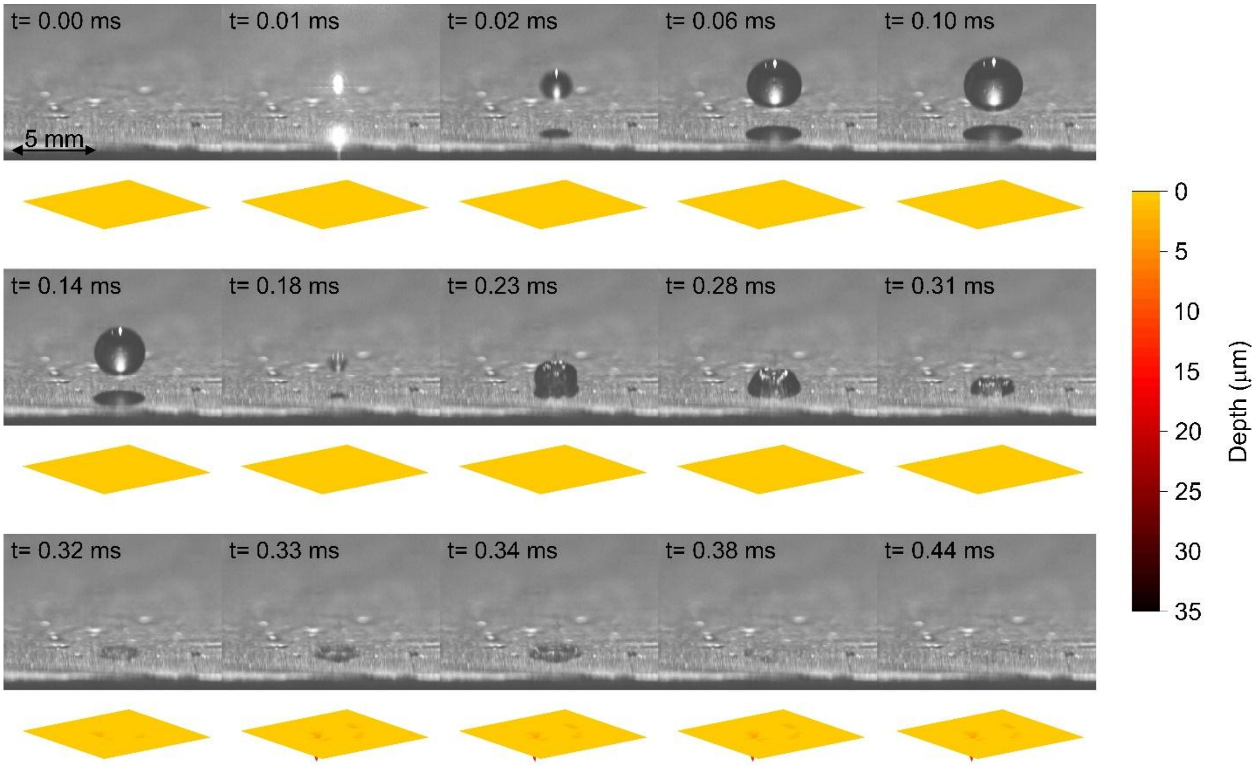

Fig. 7: Bubble and damage for collapse far away from the wall (γ =1.90).

The dynamics of the bubble is roughly the same – the same size is reached by t =0.08 ms. At t = 0.18 ms the bubble collapses in a form of a micro-jet. This still occurs far from the wall – approximately 1 mm. After the jet reaches the surface, it spreads radially outwards what causes splashing and consequent secondary collapse at t=0.32 ms. On the other hand, the dynamics of the damage differs from the previous case. No damage due to the jet is observed and the collapse of the bubble ring causes a less pronounced damage to the foil which is about 7 μm deep and corresponds to the shape of the ring before the collapse.

3.1.4 Bubble far away from the wall (γ =2.90)

Finally, the bubble was generated even further from the wall. No damage was detected in this case, hence Fig. 8 shows only the frames of bubble dynamics.

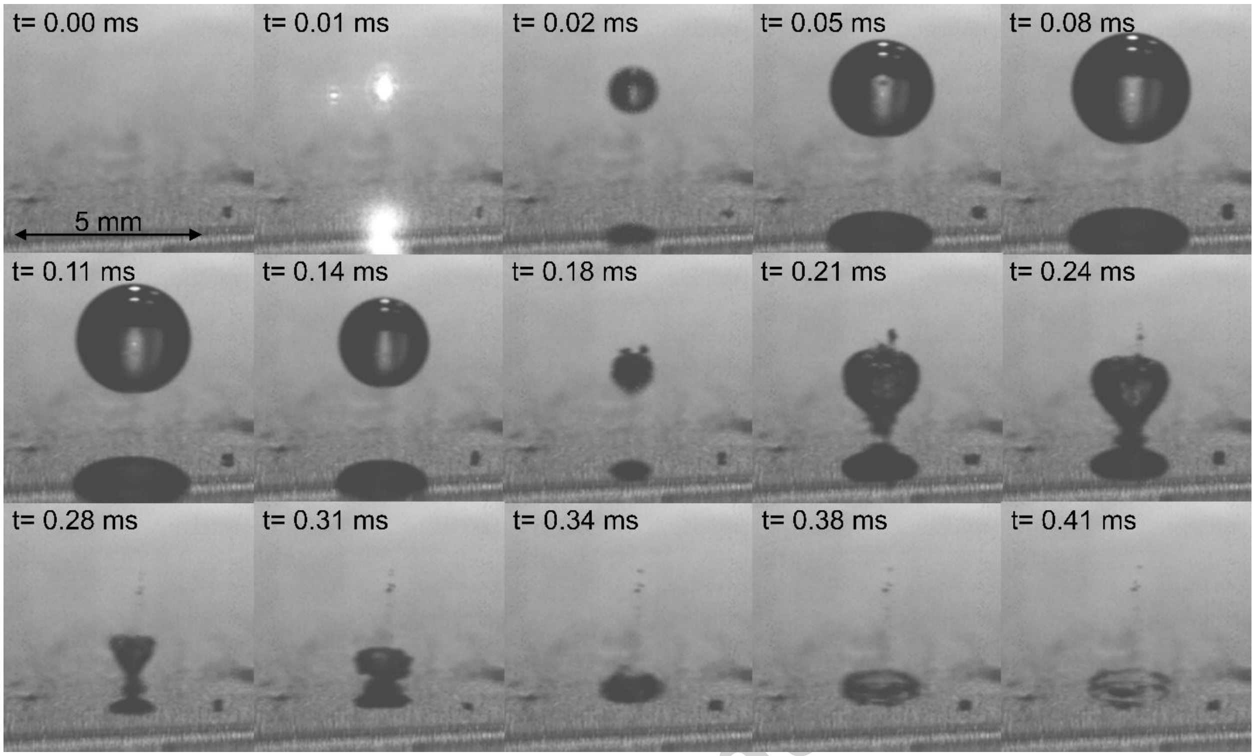

Fig. 8: Bubble collapse very far away from the wall (γ =2.90).

The size of the bubble is the same as in previous cases – it again reaches the maximum size of r=1.6 mm at t=0.08 ms. It collapses in a form of a microjet at 0.18 ms, what is followed by a secondary evaporation and consequent bubble growth, due to shear flow even as the jet travels towards the surface (t=0.21 ms). The bubble collapses for the second time in the form of the jet at t=0.28 ms, but its velocity is too small to cause any damage to the foil. Nevertheless, splashing occurs and a bubble ring collapses at about t=0.41 ms, again causing no damage to the foil.
One can also observe that in this case the ring is not in contact with the surface - seen from the double ring shadow at t=0.41 ms. Possibly this is the reason why in the case of larger γ, the ring collapse does not cause damage.

3.1.5 Further analysis of the mechanisms

Figure 9 shows the damaged volume as a function of the nondimensional distance γ of the bubble from the wall. Since our methodology discriminates between the two mechanisms, each is shown separately, so one can determine the significance of the microjet and the microbubble collapse inside the ring as a function of γ.

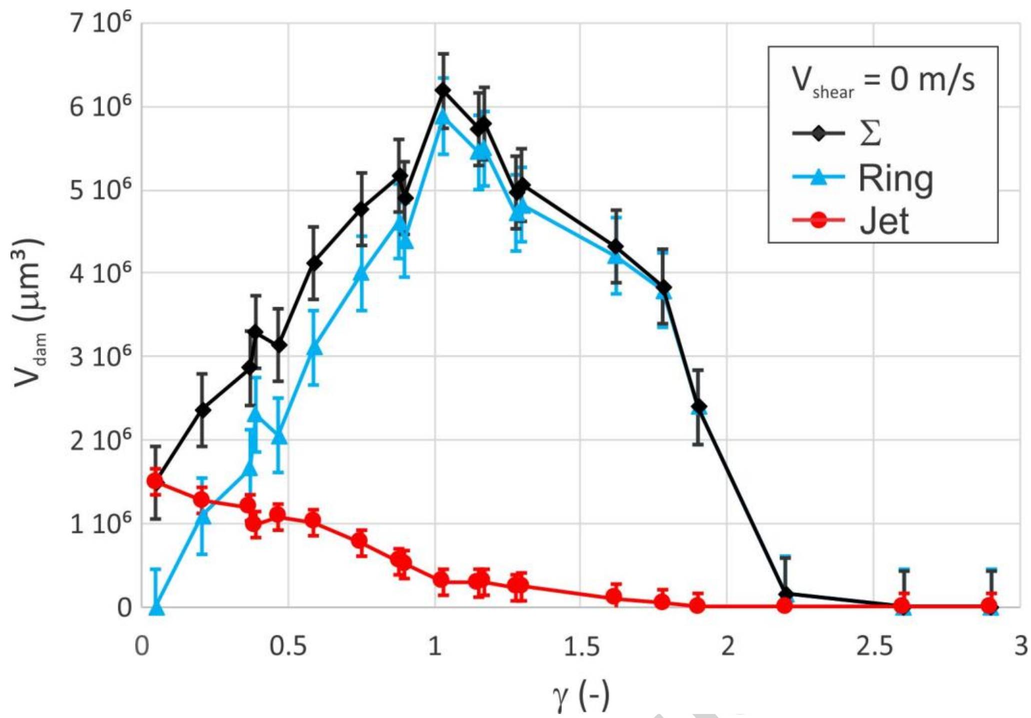

Fig. 9: Damage as a function of the distance from the wall.

The results in Fig. 9 show the significance of microjet impact and the bubble ring collapse as a function of the initial distance of the bubble from the wall. As already shown in the examples in Figs. 5-8, the damage caused by the impact of the micro-jet is most pronounced at small values of γ. Its influence is diminished at $\gamma>2$ due to the influence of the deceleration by friction as it travels towards the surface.

Also, when γ is small, the formation of the bubble ring is not pronounced (see Fig. 5). Consequently, the damage caused by the collapse of the ring after splashing is not significant when the bubble lies close to the wall. The maximal damage is caused by the collapse of the ring at about $\gamma=1$, when the splashing is most significant. At higher values of γ, the ring formation and collapse are again not as violent, due to the lower velocity of the micro-jet. Minor damage occurs for $2.0<\gamma<2.5$ and no damage is detected when $\gamma>2.5$.

3.2 Bubble in the presence of shear flow

Researchers argued in the past [10] that the presence of the shear flow may significantly alter the physics of the damage occurrence. We have tested a wide range of conditions, but no damage could be detected when γ exceeded 1.4 and there was no influence of the shear flow in the cases when γ was smaller than 0.5. In all cases (Figs. 10-13) the flow velocity was 5 m/s (from the right to the left). The velocity was chosen arbitrary to maximize the shear effect while keeping the bubble within the acquisition frame. In addition, in cavitating flows, the bulk liquid velocity is usually in the order of 20 m/s, with this value decreasing while approaching to the wall. As for the previously mentioned reasons, the value of 5 m/s was chosen. Also, there were some numerical studies published on this topic (for example [10]), where bubbles were exposed to similar velocities.

As the flow exited the nozzle it was already developed (turbulent, Re ≈ 50000) and the velocity profile was relatively homogeneous. Compared to the thickness of the jet flow, the bubble was smaller and fully immersed in it, hence the influence of the velocity profile should be minimal. Bubbles at similar conditions as the stationary ones (Figs. 5-8) are presented.

3.2.1 Bubble in a close vicinity of the wall (γ=0.10)

Figure 10 shows the collapse of a bubble in a close vicinity of the wall, which was also subjected to shear flow.

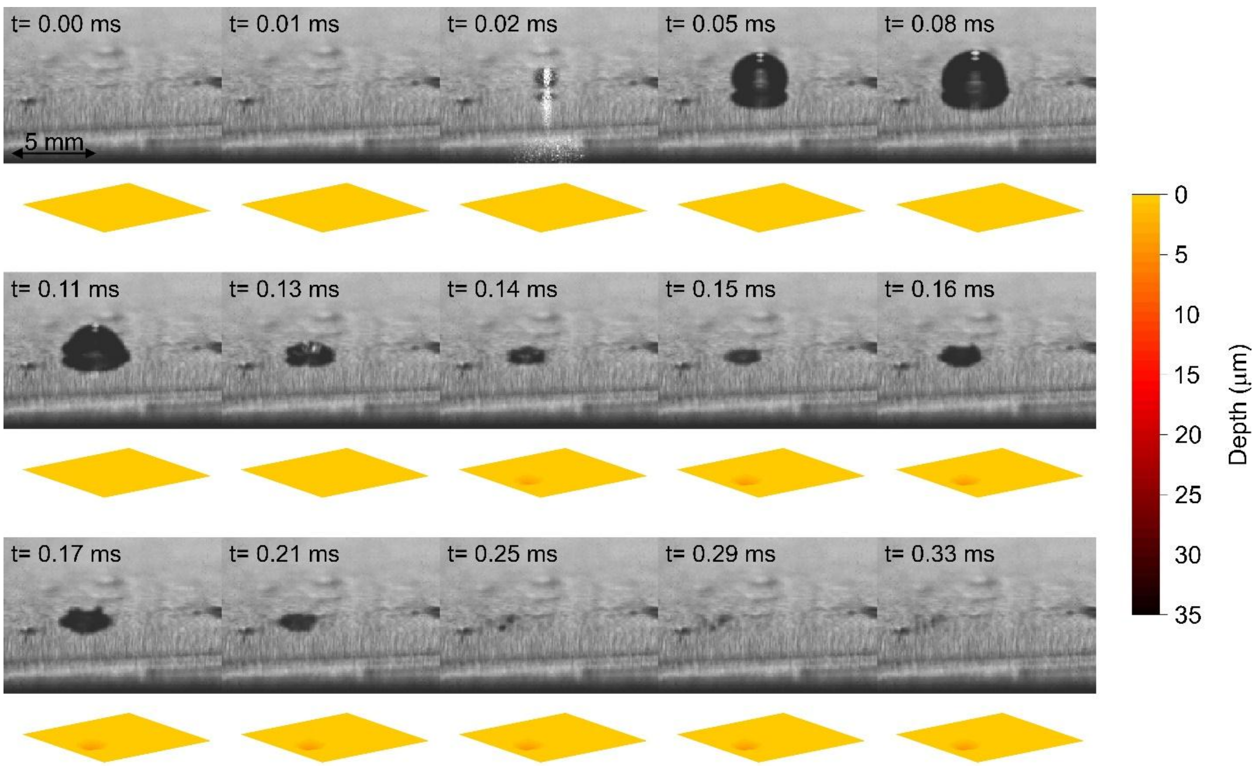

Fig. 10: Bubble and damage for collapse in the close vicinity of the wall (γ=0.10) in the presence of shear flow.

One can see that the bubble is transported by the flow. The dynamics of the bubble is not significantly influenced by the presence of the flow. It reaches its the maximal size at t=0.08 ms. Its shape is somewhat deformed (compared to the half spherical one in Fig. 5). The bubble collapses at t=0.16 ms, what causes damage to the foil. Its size and depth are comparable to the case of a stationary bubble. Roughly 0.08 ms later, the secondary collapse occurs but does not cause detectable damage.

3.2.2 Bubble in a vicinity of the wall (γ=0.95)

In the second case, the bubble was generated somewhat further from the wall. The shear flow velocity is again 5 m/s (from right to the left).

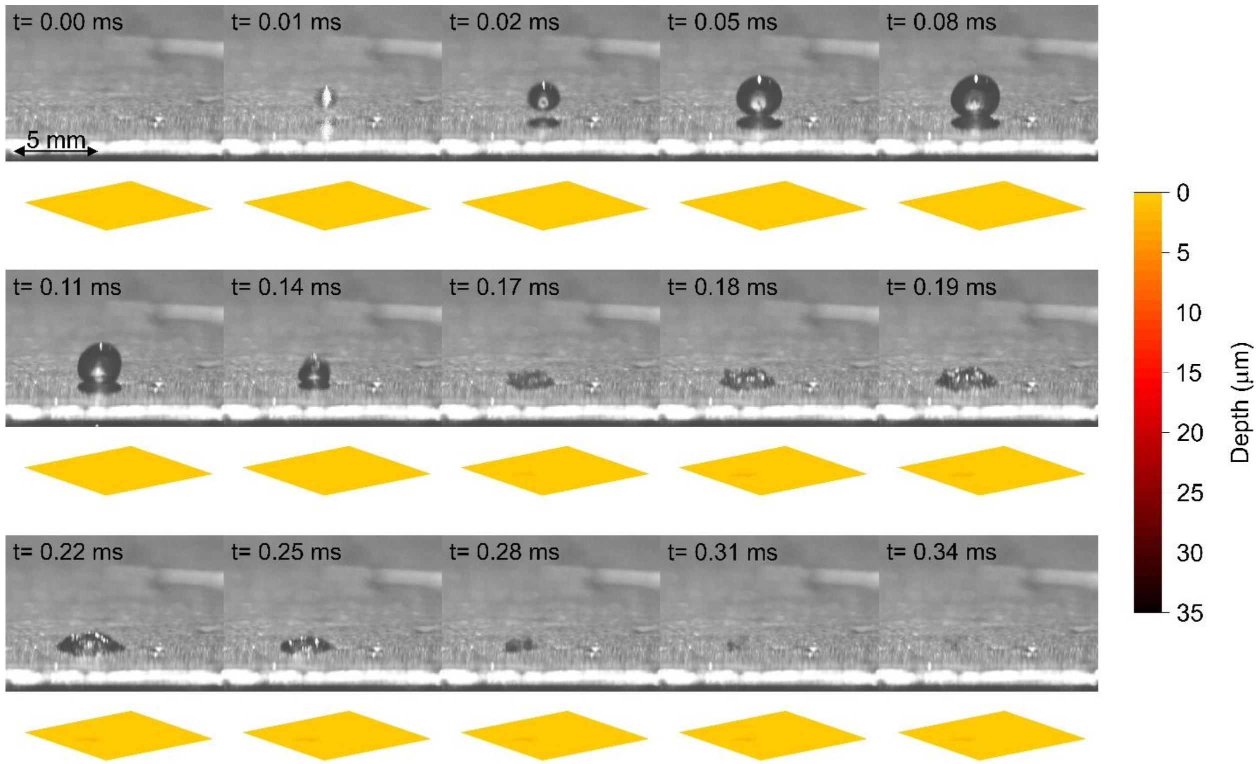

Fig. 11: Bubble and damage for collapse in the vicinity of the wall (γ=0.98) in the presence of shear flow.

The bubble is significantly deformed by the shear flow. The time dynamics remains unaltered, but the jet hits the wall at about 15° angle with respect to the normal. This, however does not diminish its effect. The damage caused by it (at t=0.17 ms) is again comparable to the one at stationary conditions (Fig. 6). The bubble then splashes, but with the presence of the flow, the collapse of the ring causes only very limited damage. This is somewhat surprising as one would expect that the micro-jet would be more susceptible to the influence of the shear flow.

3.2.3 Bubble away from the wall (γ =1.98)

Moving further away from the wall, Fig. 12 shows the results at γ=1.98. No damage was found in this case.

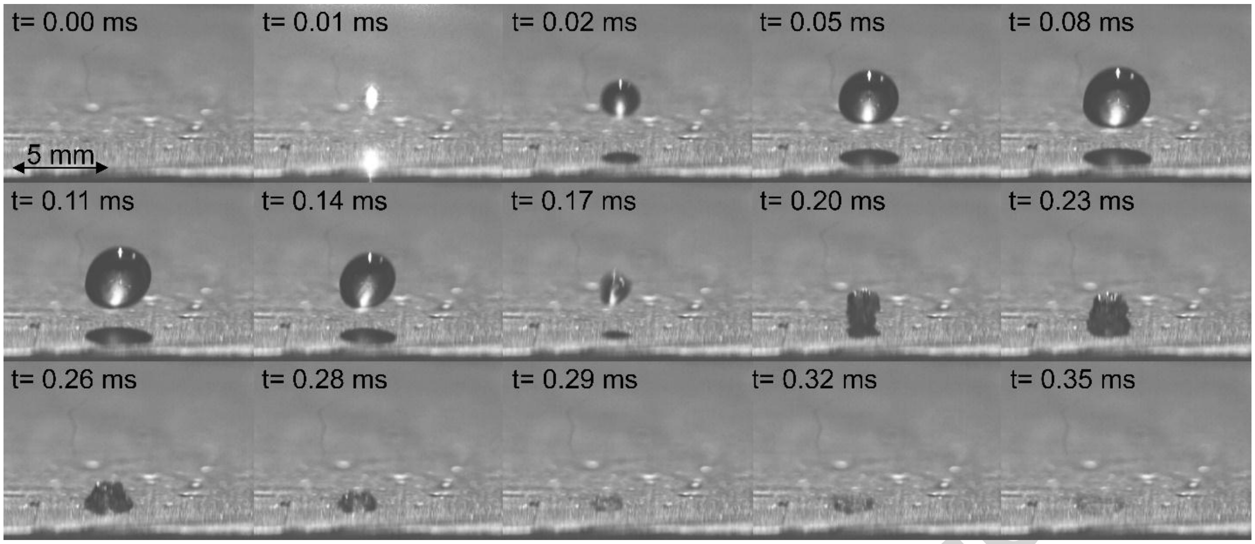

Fig. 12: Bubble collapse far away from the wall (γ =1.98) in the presence of shear flow.

The maximal size is reached at t=0.08 ms. The bubble is significantly deformed at this moment. Consequently, the micro-jet shoots at an angle of 17° to the surface with respect to the normal. As expected (based on the observations at stationary conditions), no damage was found as it hits the foil. The splashing is, due to an asymmetric collapse, not as perceptible. Consequently, the collapse is also not as intensive, and no damage was found.

3.2.4 Bubble far away from the wall (γ =2.98)

Finally, the dynamics of the bubble in the presence of the shear flow (v=5 m/s) at very large γ was observed (Fig. 13). Again, no damage was detected.

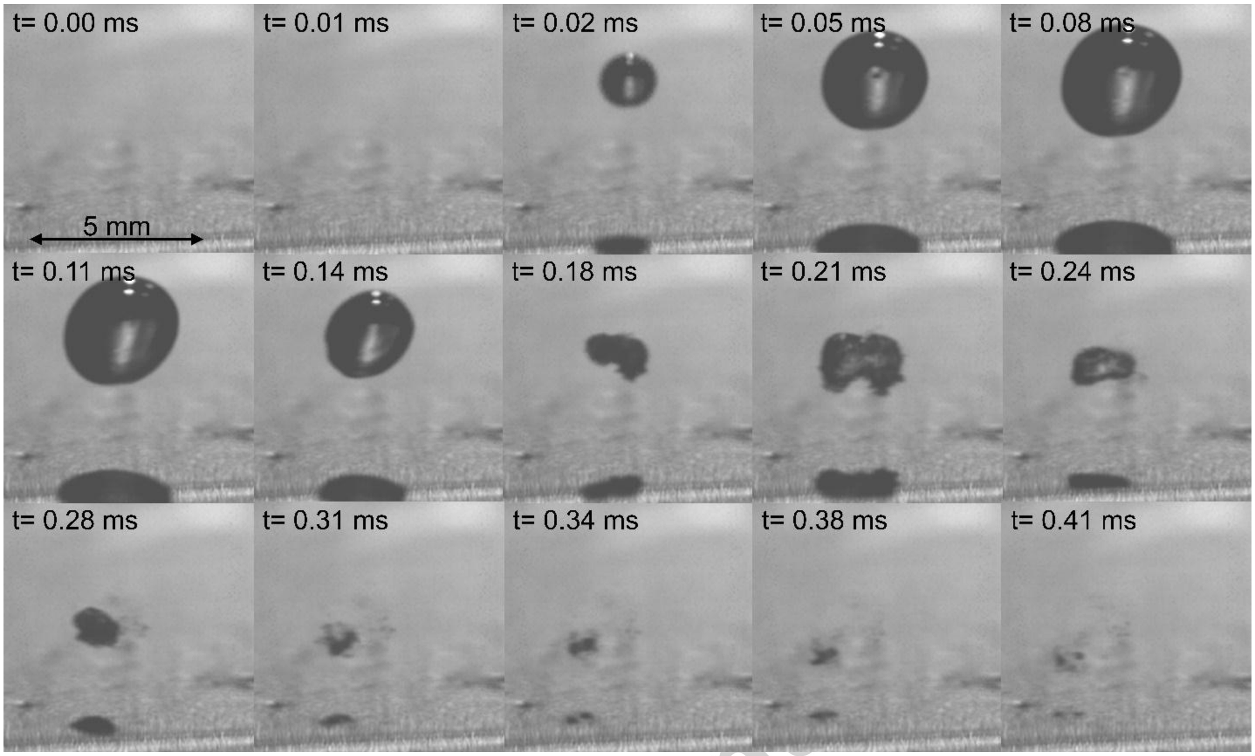

Fig. 13: Bubble collapse very far away from the wall (γ =2.98) in the presence of shear flow.

.

Similarly, to the previous cases at flowing conditions, the bubble is deformed by the flow. The collapse at t = 0.18 ms is completely asymmetric, the micro-jet is very hard to distinguish – its angle was estimated to 35° with respect to the normal. Consequently, splashing also does not occur.

3.2.5 Further analysis of the mechanisms

The diagram in Fig. 14 shows the importance of individual mechanisms as a function of the bubble distance from the wall γ.

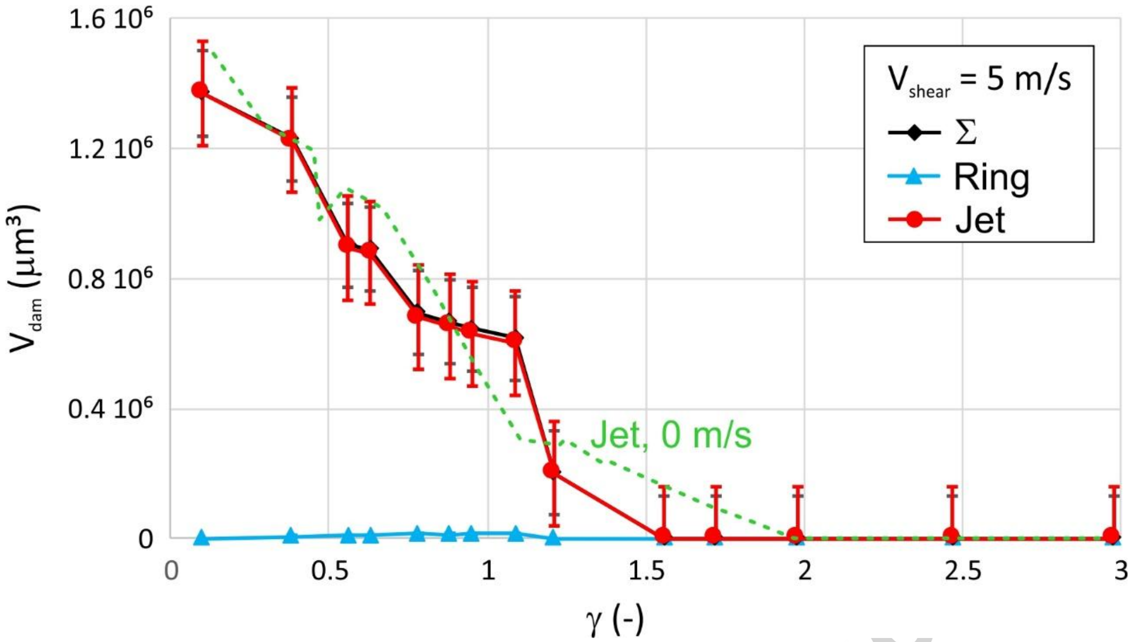

Fig. 14: Damage as a function of the distance from the wall in the presence of shear flow.

The experiments show that when the shear flow is present, the dominant damage mechanism is the micro-jet impact. This seems to be almost unaffected by its deviation from the perpendicular direction due to the shear flow (comparing the values of the jet damage for stationary and flowing cases). One must note that even at an angle of 20° (case at γ =1.98) its perpendicular component is still cos 20° = 0.93 of the total magnitude, what explains the small influence. On the other hand, this small deviation results in much less symmetric splashing (see also Fig. 18), which in term significantly reduces the effect of the collapse of bubbles in the ring. Interestingly if one compares the microjet damage for the case of no shear flow - the dotted line in Fig. 14 (extracted from Fig. 9), we there is only a slight difference. At small values of γ the flow has no effect, but it somewhat diminishes the erosive potential of the jet at larger values of γ. This is further elaborated in the discussion section.

3.3 Very high-speed observation of foil deformation

To investigate further the process of pit formation, we set the camera to its fastest framerate of 2.1 Mfps (Δt = 0.48 μs). The bubble was positioned at the non-dimensional distance of γ =0.05 (without shear flow), hence we expected a single pit resulting from the micro-jet impact. Figure 15 shows the results.

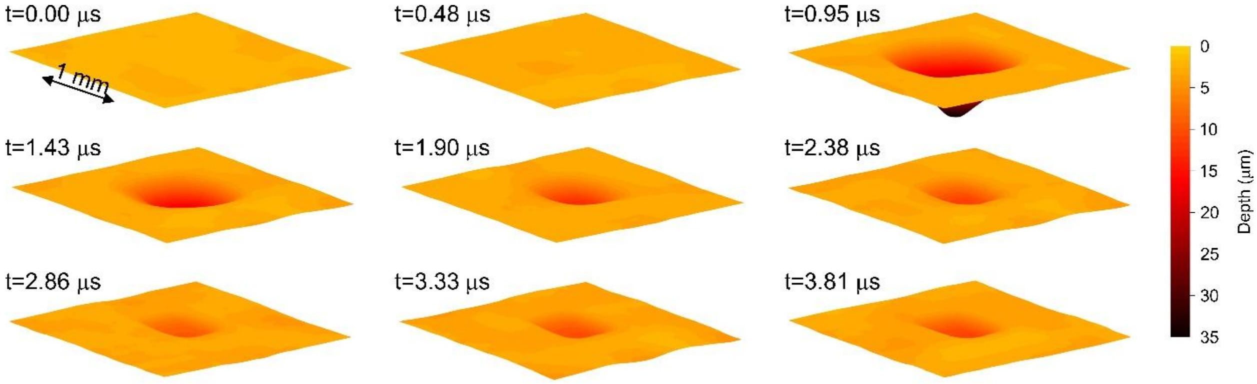

Fig. 15: Damage evolution recorded at 2.1 Mfps.

One can see that a significant pit emerges at 0.95 μs. Its depth was measured to be 35μm. Later on, the pit depth and the volume slowly reduce and the final shape (approximately 10 μm deep pit) is established about 1.5 μs after the first contact of the micro-jet and the material (at t=2.38 μs). This dynamics can be explained by the fact that the foil is firstly elastically and then plastically deformed. When the stress by the jet is reduced, the materials relaxes and only the plastic deformation is preserved.

This is again shown in Fig. 16 in terms of the pit volume as a function of time.

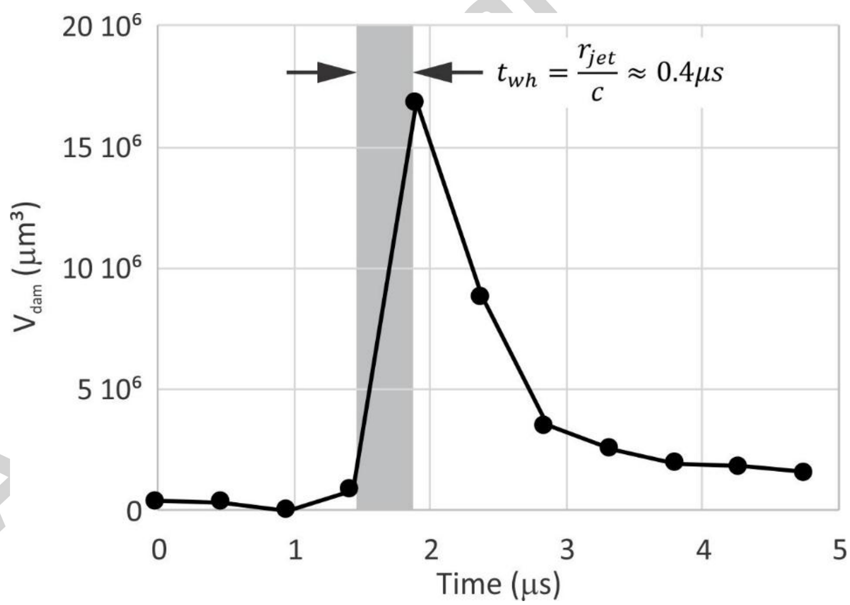

Fig. 16: Time evolution of pit volume.

The deformation of the foil due to jet impact occurs in an extremely short period of time – during less than 0.5 μs.

This corresponds well with the period during which the water hammer pressure is present at the micro-jet impact. The duration of the water hammer stress ($p_{wh} = \rho c v$) is as long as the time for the impact signal to traverse the radius of the jet ($t_{wh} = \frac{r_{jet}}{c}$), which in the present case results in approximately 0.4 μs. After that time, a stagnation pressure ($p_s = \frac{\rho v^2}{2}$) is established, which is an order of magnitude smaller than the water hammer pressure.

4 Discussion

The results show that the shear flow influences the erosive potential of the bubble collapse. Interestingly this occurs through the diminishing the effect of the ring collapse and not by the influence on the aggressiveness of the micro-jet impact - in fact the influence of the shear flow on the aggressiveness of the microjet is insignificant.

This can be explained by the analyses of the velocity, the angle and the traveled distance of the jet before it hits the solid surface.

The maximal velocity of the micro-jet can be estimated from the images in the sequence, as can be its angle and the distance with respect to the surface. For the shown cases, these are given in Tab. 1.

Tab. 1: Measured parameters of the micro-jet.

γ	v_{shear} (m/s)	Mechanism	v_{jet} (m/s)	α (°)	l (mm)	v_{imp} (m/s)
0.05	0	Jet	52	90	0	52
0.90	0	Jet & Ring	92	90	0	92
1.90	0	Ring	125	90	1.8	27
2.90	0	-	175	90	2.7	10
0.10	5	Jet	48	88	0	47
0.98	5	Jet	75	79	0	73
1.98	5	-	120	73	2.2	13
2.98	5	-	140	55	3.4	2

We see in Tab. 1 that the jet velocity (v_{jet}) does not change significantly when even a strong shear flow (v_{shear}) is present – in average about 15%. Also, the jet angle (α) is influenced significantly only at larger distances of the bubble from the wall (l). Hence it is expected that also the velocity perpendicular to the surface will be significantly diminished only at larger distances. The final influential parameter is the distance the jet needs to travel before it touches the wall. Friction reduces its velocity (component perpendicular to the surface) at impact (v_{imp}), which was again estimated from the images.

If one calculates the water hammer pressure at the impact of the micro-jet $p_{mj} = \eta \cdot \rho \cdot c \cdot v$ [7], we can determine the stress on the material (Fig. 17).

The subsequent formation and collapse of the bubble ring is governed by the dynamics, which can be approximated by the Gilmore's equation (Eqn. 5) [22]. This is mainly due to the fact that the bubbles inside the ring are small and likely preserve spherical shape during the collapse.

$$R\ddot{R}\left(1-\frac{\dot{R}}{c}\right)+\frac{3}{2}\dot{R}^2\left(1-\frac{\dot{R}}{3c}\right)=H\left(1+\frac{\dot{R}}{c}\right)+\frac{R\dot{H}}{c}\left(1-\frac{\dot{R}}{c}\right) \quad (5)$$

Here R represents the spherical bubble radius, c is the speed of sound in water, and H the enthalpy difference between the state at the outer side of the bubble wall and the reference state.

We have considered both, c and H, according to Gilmore's formulation without the subsonic approximation [22]. Internal bubble pressure was calculated using the adiabatic law for ideal gasses. Effects of both the surface tension and viscosity were considered.

In our calculations, we assumed that the initial bubble nucleus has a radius of 40 µm, which lies just under the resolution of the images (50 µm/pixel). The pressure evolution is estimated from the velocity of the micro-jet impact, which drives the formation of the bubble ring, and is given in Eqn. 6.

$$p_\infty\,(t) = \begin{cases} 10^5\,Pa;\;\; t \leq 1ms \\ 10^5\,Pa - \frac{\rho v_{imp}^2}{2};\;\; 1ms < t \leq 1ms + \frac{R_{ring}}{v_{imp}} \\ 10^5\,Pa;\;\; t > 1ms + \frac{R_{ring}}{v_{jet}} \end{cases} \quad (6)$$

We considered temporal variation of p_∞ in the time derivative of enthalpy difference $\dot{H}$, according to Kreider et al. [23]. Pressure and velocity fields were calculated as functions of time and radial distance according to Gilmore's second order approximation [22].

Figure 17 shows the calculated pressures from the micro-jet p_{mj} impact (blue) and ring collapse p_{ring} (at the radial distance of the maximal radius $r=R_{max}$ of the bubble's evolution, blue). The experimental images in the diagrams represent the actual damage for a specific value of γ. The above diagram (Fig. 17a) shows the case without the shear flow, while in the bottom (Fig. 17b) the shear is present. The dotted lines represent the approximate yield stress σ_y and ultimate tensile stress σ_{uts} of the material [24].

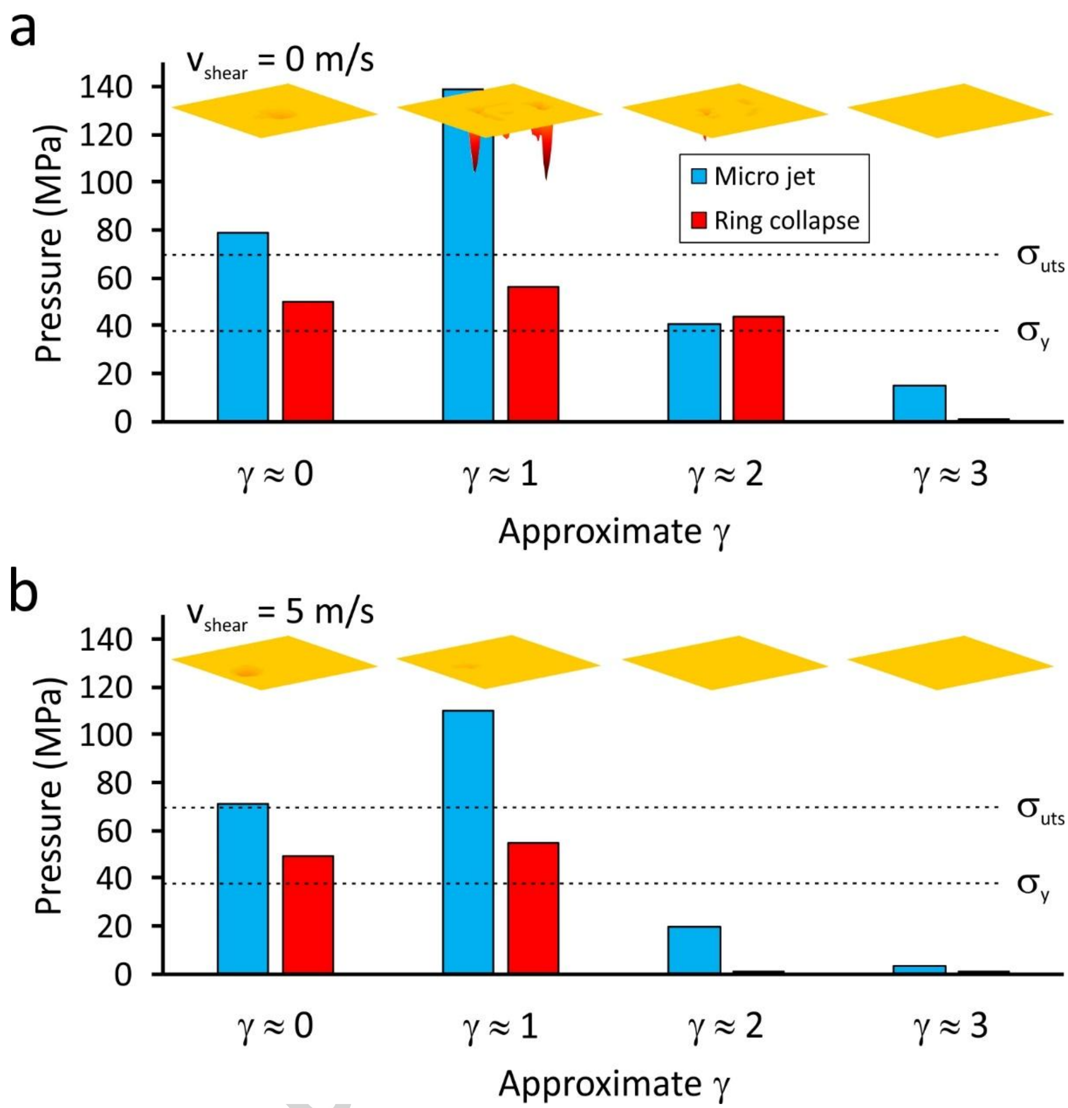

Fig. 17: Simulated pressures, which are induced by micro-jet impact and subsequent shock wave that originates from the ring collapse.

One can see that the impact of the jet, which results in the stress exceeding about 80 MPa damages the surface. This can be nicely seen for $\gamma \approx 0$ and 1 for both the case without and with the shear flow present. This incidentally fits very well to the measurements [24], where yield stress was determined to be $\sigma_y = 38.2 \pm 1.2$ MPa and ultimate tensile stress $\sigma_{uts} = 69.22 \pm 2.7$ MPa. These values however, are a result of static loading tests, and their use might be unjustified in cavitation erosion research, where the deformation occurs at a very high rate. Hence, they only serve as an orientation value here.

Similarly, the simulated shock wave pressures from the spherical bubble collapse exceed the yield stress of the material at $\gamma \approx 0$, 1 and 2 (without the presence of the shear flow) and at $\gamma \approx 0$ and 1 (with the presence of the shear flow). This again fits relatively well to the observed damage pattern. For the case of the smallest distance ($\gamma \approx 0$) the ring actually never developed (Figs. 5 and 10), hence it cannot cause damage.

As for the case of $\gamma \approx 1$ and with the presence of shear flow, the shape of the ring is significantly distorted, and its collapse is incoherent (seen already in Fig. 11 and again from the bottom view, through a transparent glass plate, in Fig. 18).

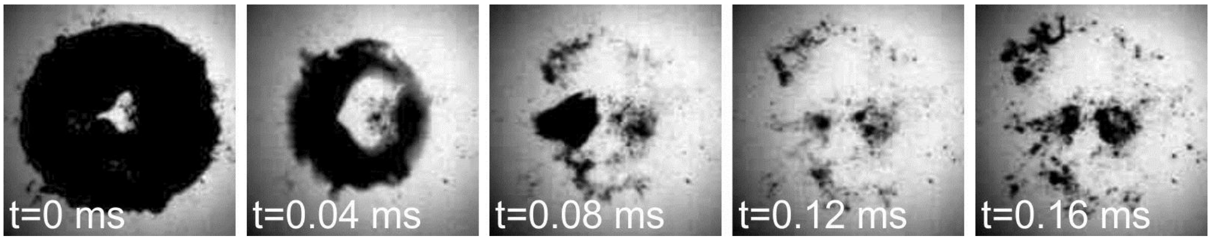

Fig. 18: Asymmetrical and incoherent collapse of the bubble ring (γ =0.98, v =5 m/s)

The presence of the shear flow (from right to the left) causes the ring to collapse first on the upstream (right) side, which might be the reason for the negligible damage caused by its collapse.

We can see that the calculation (Fig. 17) correctly predicts the insignificance of the microjet impact and the shock wave for the cases at larger distances from the wall.

5 Conclusions

In the study we investigated the last stage in the cascade of events that lead to the occurrence of cavitation damage – single bubble collapse and the resulting deformation of the material.
By the simultaneous observation of the bubble dynamics and the deformation of a thin aluminum foil employing two high speed cameras we were able to directly observe the process.
Various distances of the bubble from the specimen were investigated. We also observed the collapse of a bubble in the presence of shear flow – this was essential, since many researchers claim that the presence of a pressure gradient diminishes the erosive potential of the micro-jet.
Based on an ensemble of measurements we can conclude that:

- when cavitation bubble implodes near the wall (γ<0.2), the most pronounced mechanism is the impact of the micro-jet;
- when the bubble collapses further away from the wall (γ>0.5), the influence of the micro-jet diminishes and the collapse of microscopic bubbles in the rebounded cloud (ring) is more important;
- finally, in the cases where the shear flow was introduced, the bubbles near the wall behaved in the same way as without the presence of the flow (micro-jet mechanism was the driving one). In the mid-range of distances (0.5< γ <1.4) the micro-jet was still the most important mechanism, but some minor damage was also induced by the secondary (ring) collapse, and further away from the wall, the deflection of the micro-jet was too large to cause either damage or rebound of the bubble.

Further on we observed the formation of a pit at the highest framerate setting of the camera and concluded that the damage indeed results from the water hammer pressure at micro-jet impact and that one can also observe deformation and relaxation of the material by this methodology.

The work represents one of the final "pieces of the puzzle", which will lead to a detailed understanding of the cavitation erosion process and will enable the development of the models for the prediction of cavitation damage.

Acknowledgments
The authors acknowledge the financial support from the Slovenian Research Agency (research core Funding No. P2-0401, No. P2-0270 and No. P2-0392 and Projects No. J2—6774, No. L2-8183, No. L2-9240 and No. L2-9254). The article is in part the result of work in the implementation of the SPS Operation entitled Building blocks, tools and systems for future factories—GOSTOP.

References

[1] J. T. Bark, G, Friesch, J., Kuiper, G., Ligtelijn, "Cavitation Erosion on Ship Propellers and Rudders," in *9th Symposium on Practical Design of Ships and Other Floating Structures, Luebeck-Travemuende Germany*, 2004.

[2] M. Dular, B. Stoffel, and B. ?irok, "Development of a cavitation erosion model," *Wear*, vol. 261, no. 5–6, 2006.

[3] R. Fortes-Patella, J.L. Reboud, and L. Briancon-Marjollet, "A phenomenological and numerical model for scaling the flow aggressiveness in cavitation erosion," *EROCAV Workshop, Val de Reuil*, 2004.

[4] R. P. Tong, W. P. Schiffers, S. J. Shaw, J. R. Blake, and D. C. Emmony, "The role of 'splashing' in the collapse of a laser-generated cavity near a rigid boundary," *Journal of Fluid Mechanics*, vol. 380, p. S0022112098003589, Feb. 1999.

[5] J. R. Blake and D. C. Gibson, "Cavitation Bubbles Near Boundaries," *Annual Review of Fluid Mechanics*, vol. 19, no. 1, pp. 99–123, Jan. 1987.

[6] M. S. Plesset and R. B. Chapman, "Collapse of an initially spherical vapour cavity in the neighbourhood of a solid boundary," *Journal of Fluid Mechanics*, vol. 47, no. 2, p. 283, May 1971.

[7] G. L. Chahine, "Modeling of Cavitation Dynamics and Interaction with Material," in *Advanced Experimental and Numerical Techniques for Cavitation Erosion Prediction. Fluid Mechanics and Its Applications 106. Edts.: Kim, K.H., Chahine, G., Franc, J.P., Karimi, A., Springer*, 2014, pp. 123–161.

[8] I. Hansson, V. Kedrinskii, and K. A. Morch, "On the dynamics of cavity clusters," *Journal of Physics D: Applied Physics*, vol. 15, no. 9, pp. 1725–1734, Sep. 1982.

[9] A. Philipp and W. Lauterborn, "Cavitation erosion by single laser-produced bubbles," *J. Fluid Mech*, vol. 361, pp. 75–116, 1998.

[10] P. Yu, S. L. Ceccio, and G. Tryggvason, "The collapse of a cavitation bubble in shear flows—A numerical study," *Physics of Fluids*, vol. 7, no. 11, pp. 2608–2616, Nov. 1995.

[11] ASTM G32-16, "Standard Test Method for Cavitation Erosion Using Vibratory Apparatus," *ASTM International, West Conshohocken, PA, 2016, www.astm.org*, 2016.

[12] M. Petkovsek and M. Dular, "Simultaneous observation of cavitation structures and cavitation erosion," *Wear*, vol. 300, no. 1–2, 2013.

[13] M. Dular and M. Petkovsek, "On the mechanisms of cavitation erosion - Coupling high speed videos to damage patterns," *Experimental Thermal and Fluid Science*, vol. 68, 2015.

[14] A. Jayaprakash, S. Singh, and G. L. Chahine, “Experimental and Numerical Investigation of Single Bubble Dynamics in a Two-Phase Bubbly Medium,” *ASME Journal of Fluids Engineering*, vol. 133, no. 12, pp. 121305-1-121305–9, 2011.
[15] J. Ma, G. L. Chahine, and C. Hsiao, “Spherical bubble dynamics in a bubbly medium using an Euler – Lagrange model,” *Chemical Engineering Science*, vol. 128, pp. 64–81, 2015.
[16] Ruo Zhang, Ping-Sing Tsai, J. E. Cryer, and M. Shah, “Shape-from-shading: a survey,” *IEEE Transactions on Pattern Analysis and Machine Intelligence*, vol. 21, no. 8, pp. 690–706, 1999.
[17] M. Dular, O. C. Delgosha, and M. Petkov?ek, “Observations of cavitation erosion pit formation,” *Ultrasonics Sonochemistry*, vol. 20, no. 4, 2013.
[18] M. Dular, B. Bachert, B. Stoffel, and B. ?irok, “Relationship between cavitation structures and cavitation damage,” *Wear*, vol. 257, no. 11, 2004.
[19] B. Horn and M. J. Brooks, *Shape from shading*. MIT Press, 1989.
[20] M. Harker and P. O’Leary, “Least squares surface reconstruction from measured gradient fields,” in *2008 IEEE Conference on Computer Vision and Pattern Recognition*, 2008, pp. 1–7.
[21] P. De Groot and D. Fitzgerald, “Measurement, certification and use of step-height calibration specimens in optical metrology Measurement, certification and use of step-height calibration specimens in optical metrology,” *Paper 10329-44, SPIE Optical Metrology, June 2017, Munich,Germany*, no. June, 2017.
[22] F. R. Gilmore, “The growth or collapse of a spherical bubble in a viscous compressible liquid,” Hydrodynamics Laboratory, California Institute of Technology , Pasadena, CA., 1952.
[23] W. Kreider, L. A. Crum, and M. R. Bailey, “A reduced-order , single-bubble cavitation model with applications to therapeutic ultrasound,” vol. 130, no. November, pp. 3511–3530, 2011.
[24] C. Malmberg and B. Kack, “Aluminium foil at multiple length scales, mechanical tests and numerical simulations in Abaqus,” *Division of Solid Mechanics, Media-Tryck AB, Lund, Sweden*, 2015.

Highlights:

- Cavitation damage from a single bubble was observed
- Pit formation during 3μs was measured
- Shear flow influence on erosion was determined
- Importance of microjet and shock wave was determined